

SOFT ROBOTS

Voxelated three-dimensional miniature magnetic soft machines via multimaterial heterogeneous assembly

Jiachen Zhang^{1†}, Ziyu Ren^{1,2†}, Wenqi Hu^{1†}, Ren Hao Soon^{1,2}, Immihan Ceren Yasa¹, Zemin Liu^{1,2}, Metin Sitti^{1,2,3*}

Copyright © 2021
The Authors, some
rights reserved;
exclusive licensee
American Association
for the Advancement
of Science. No claim
to original U.S.
Government Works

Small-scale soft-bodied machines that respond to externally applied magnetic field have attracted wide research interest because of their unique capabilities and promising potential in a variety of fields, especially for biomedical applications. When the size of such machines approach the sub-millimeter scale, their designs and functionalities are severely constrained by the available fabrication methods, which only work with limited materials, geometries, and magnetization profiles. To free such constraints, here, we propose a bottom-up assembly-based 3D microfabrication approach to create complex 3D miniature wireless magnetic soft machines at the milli- and sub-millimeter scale with arbitrary multimaterial compositions, arbitrary 3D geometries, and arbitrary programmable 3D magnetization profiles at high spatial resolution. This approach helps us concurrently realize diverse characteristics on the machines, including programmable shape morphing, negative Poisson's ratio, complex stiffness distribution, directional joint bending, and remagnetization for shape reconfiguration. It enlarges the design space and enables biomedical device-related functionalities that are previously difficult to achieve, including peristaltic pumping of biological fluids and transport of solid objects, active targeted cargo transport and delivery, liquid biopsy, and reversible surface anchoring in tortuous tubular environments notwithstanding fluid flows, all at the sub-millimeter scale. This work improves the achievable complexity of 3D magnetic soft machines and boosts their future capabilities for applications in robotics and biomedical engineering.

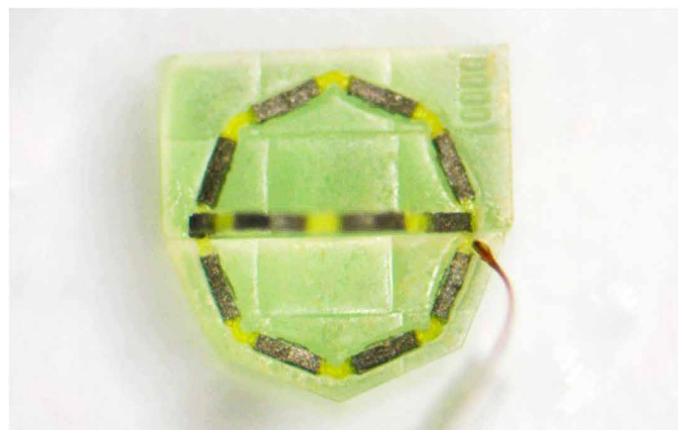
INTRODUCTION

Small-scale soft-bodied machines that respond to external stimuli may lead to bioinspired robotics (1–5) and applications involving robotic manipulation (6–8). Particularly, wireless and soft micro-robots are exciting candidates for biomedical applications (9–12). The application of external magnetic fields is a promising choice for safe, fast, precise, and dexterous actuation of these machines (13–16). Although recent studies have advanced the fabrication of small-scale magnetic soft machines substantially, the integration of multiple arbitrary material compositions with arbitrary 3D magnetic programming and geometry for small-scale soft machines still remains an open scientific challenge. Moreover, the existing methods—i.e., two-dimensional (2D) mold casting and laser cutting (17–22), extrusion- (16) and ultraviolet (UV) lithography-based (13, 23) 3D printing, and chemical self-assembly or synthesis (24, 25)—suffer from some fundamental constraints that prevent them from being further improved. Specifically, the extrusion-based approaches (16) cannot fabricate finer magnetic soft fibers to weave complex structures because of the demanding requirement of storage modulus, the deterioration of performance caused by the added magnetic particles, and the extrudate swell (26) of the soft elastomers. The strong local interaction of magnetic particles inside uncured liquid photoresists restricts programming arbitrary magnetization of neighboring voxels by lithography-based approaches (13).

The functionality of a magnetic soft machine is dictated by its magnetic components and their magnetization profiles, which introduce local 3D shape deformations on the soft machine by the externally controlled 3D magnetic fields. For any individual device

that has been reported, its magnetic component has so far been made of a single kind of magnetic composite material, i.e., a single kind of base material with a single kind of embedded magnetic particles at a fixed concentration. A lack of fabrication capability of existing approaches causes the existing devices to be severely limited in material selection (often just one homogeneous material), geometry design (often simple 2D or 3D shapes), and magnetization programmability (coupling with geometry, chaining, and/or constant strength). All these constraints limit the design space, miniaturization, and functions of the current soft machines. They also prevent the physical realizations of theoretically promising designs or force them to be compromised in functionalities.

In view of these challenges, we propose to use a jig-assisted 3D heterogeneous integration approach to assemble microscale building blocks, which are called “voxels” hereafter, to fabricate small-scale



Movie 1. Overview of the jig-assisted 3D heterogeneous integration approach for small-scale wireless magnetic soft-bodied machines.

¹Physical Intelligence Department, Max Planck Institute for Intelligent Systems, 70569 Stuttgart, Germany. ²Institute for Biomedical Engineering, ETH Zurich, 8092 Zurich, Switzerland. ³School of Medicine and College of Engineering, Koç University, 34450 Istanbul, Turkey.

*Corresponding author. Email: sitti@is.mpg.de

†These authors contributed to this work as co-first authors.

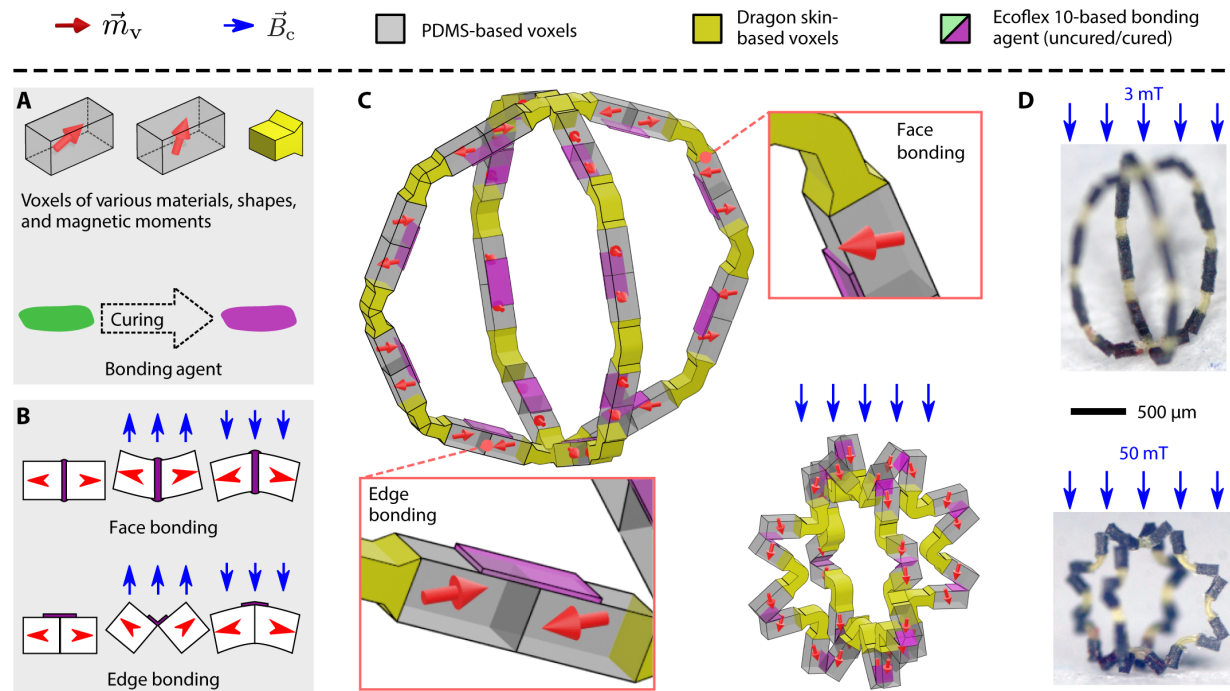


Fig. 1. The proposed jig-assisted heterogeneous integration approach for 3D fabrication of small-scale magnetic soft machines. (A) Voxels with different materials, shapes, and magnetization profiles \vec{m}_v were integrated together by a bonding agent to build soft machines. (B) Bonding agent was applied to connect neighboring voxels in two different ways: face bonding and edge bonding, which respond to the external magnetic field \vec{B}_c differently. (C) An example soft machine with two interconnected circular rings was fabricated by assembling several heterogeneous voxels at designated 3D positions and orientations. The insets show the places where two bonding options were used. The bonding agent in face bonding connections is omitted in all schematics for easier visibility. (D) The fabricated soft machine experimentally showed 3D mechanical metamaterial characteristic of having a negative Poisson's ratio, consistent with the designed shape-morphing behavior.

magnetic soft machines with nonmagnetic and magnetic multimatials, 3D complex geometry and magnetic programming, and 3D-to-3D shape morphing (Movie 1). Therefore, this approach enlarges the machine design space and enhances the machine functionality substantially (table S1). It enables the creation of functional machines with complex designs that are tailored to specific biomedical applications.

RESULTS

A soft machine based on two interconnected circular rings (Fig. 1) is used to describe the proposed fabrication approach. Each ring has an outer diameter of 1.68 mm and consists of voxels that were made of three kinds of elastomers with different material properties: Dragon Skin (Smooth-On), Ecoflex 0010 silicone rubber (Smooth-On), and polydimethylsiloxane (PDMS; Sylgard 184, Dow Corning). These voxels of diverse magnetic and nonmagnetic soft materials with various geometric and material properties were batch-fabricated using soft lithography techniques (see the “Voxel fabrication” section and fig. S1). Magnetic voxels, made of soft elastomers (e.g., silicone rubber) with embedded hard magnetic microparticles (MMPs; e.g., NdFeB microparticles), bear designed individual magnetic moments \vec{m}_v (variable in both magnitude and orientation). An overall 3D magnetization profile was programmed by the heterogeneous arrangement of these magnetic voxels.

Voxels, whether magnetic or not, were integrated together with bonding agents (i.e., liquid noncross-linked soft elastomers), which

were applied to connect neighboring voxels on their faces or edges for different shape-morphing behaviors (see the “Jig-assisted assembly” section, Fig. 1B, and fig. S3). Assistant jigs were used in the fabrication process to provide guideline and reference, resulting in controlled fabrication precision and repeatability (see the “Jig-assisted assembly” section and section S2). The programmed 3D geometry and magnetization profile of this device can be seen in Fig. 1C. The fabrication process details are visualized in Fig. 2, fig. S11, and movie S1. When an external uniform magnetic field \vec{B}_c ($|\vec{B}_c| = 50$ mT) was applied, each ring shrunk in its radial direction, and the whole soft machine behaved as a 3D mechanical metamaterial with a negative Poisson's ratio (Fig. 1D).

The reported fabrication approach enables tunable magnetic moment on individual voxels down to 35 μm and arbitrary magnetization independent of geometry. A checkerboard was made by four cubic voxels with 35- μm side lengths (Fig. 3A). We define the resolution to be the 3D size of the smallest voxel that could be assembled precisely and repeatedly, whose material and magnetic properties could be varied. \vec{m}_v of each voxel can point to an arbitrary 3D direction (Fig. 3B). Besides, \vec{m}_v of relatively large voxels could be spatially varying via assuming a predeformation in the magnetizing step (20). $|\vec{m}_v|$ can range from zero to a maximum value capped by the MMPs' properties. The measured magnetization values of voxels with different MMP mass ratios (0.0, 33.3, 50.0, and 66.7%) are shown in Fig. 3C, together with the theoretical numbers (section S1). These available variations in \vec{m}_v , together with the heterogeneous assembly process, enable the creation of highly

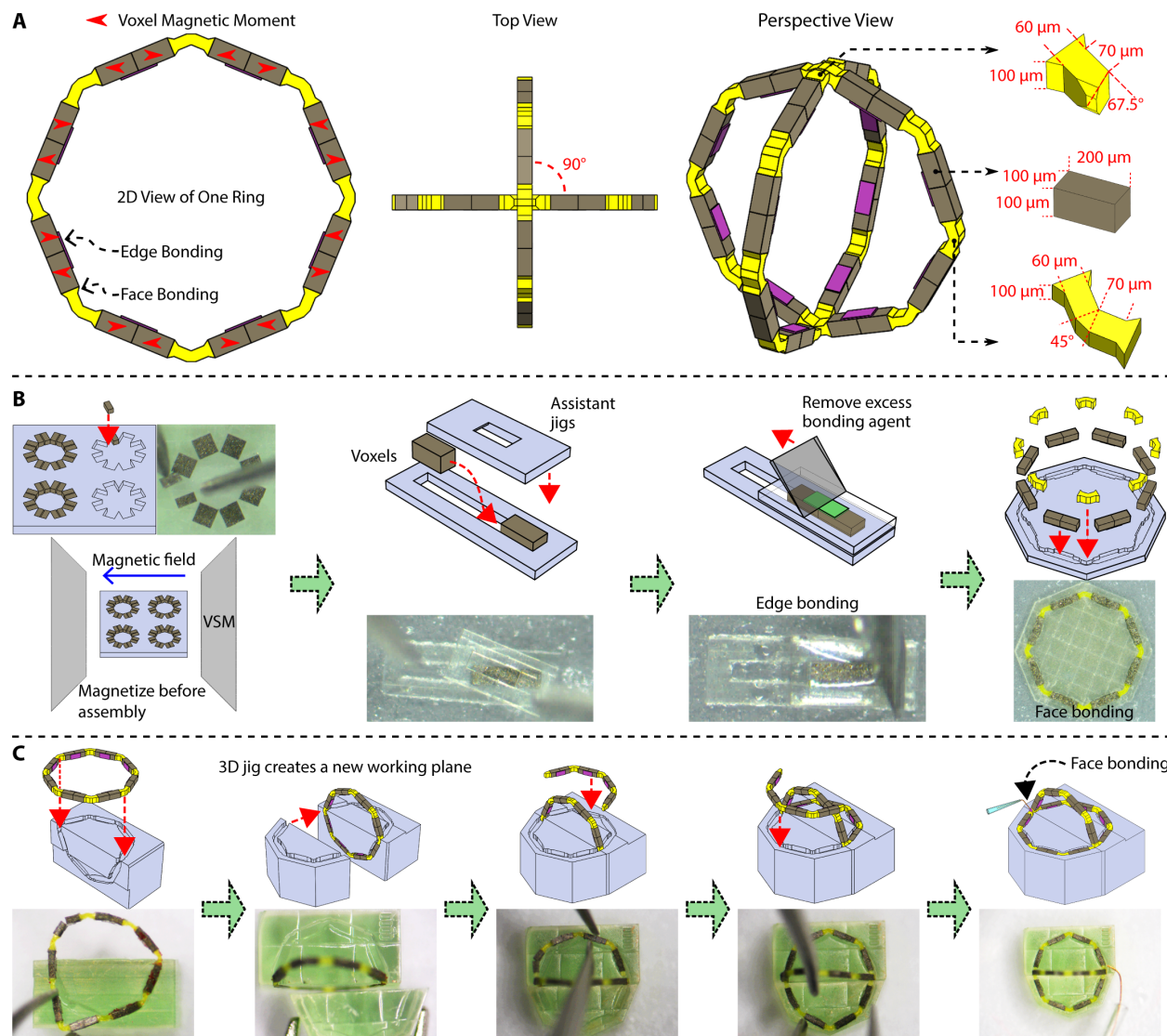


Fig. 2. Illustration of the jig-assisted fabrication of the exemplar 3D ring. (A) Designs of the ring and its voxels. **(B)** Designs of the assistant jigs and schematics of the fabrication approach with experimental photographs. A VSM was used to magnetize the voxels in desired directions and magnitudes with a controlled uniform magnetic field up to 1.8 T. The jig for edge bonding has a long slit, to avoid the strong magnetic interaction between the voxels when plugging them into the jig. Bonding agent was applied through the cap opening to form the edge bonding. Next, magnetic and nonmagnetic voxels were plugged into a 2D jig fabricated by TPP or mold casting. They were assembled by face bonding to form a (half) ring. **(C)** The ring and two half rings were plugged into a 3D jig (fabricated by TPP-based 3D microprinting) and assembled to create a 3D soft machine by face bonding.

complex overall magnetization profiles on the bodies of the fabricated machines for achieving sophisticated shape-morphing behaviors.

The reported fabrication approach can program high-fidelity 3D magnetization profiles with abrupt changes on 3D devices down to the voxel-scale level, as showcased by a hollow cube made of 218 100-µm side-length cubic voxels (Ecoflex 0050 with embedded NdFeB MMPs at 1:1 mass ratio) (Fig. 3D). Out-of-plane abrupt changes in the magnetization profile are challenging to achieve using previous 3D printing methods (13, 16), because the premagnetized MMPs used in these methods tend to stay within the 2D geometric plane and prefer to avoid abrupt direction changes due to local interactions. Moreover, fabricating a fully sealed hollow structure is

challenging using previous methods, because printing the top surface requires a supporting material and the uncured photoresist cannot be drained out afterward. In contrast, the hollow cube made with our approach has an encoded letter or symbol, i.e., “MPI-IS,” in the magnetization profile of each of its faces. The programmed magnetization profiles showed clear abrupt changes between adjacent voxels under the inspection of a magnetic field imaging instrument.

This approach enables a number of critical design features of soft tiny machines that were challenging to achieve before (13, 16, 20, 22, 27). These design features are elaborated in the following paragraphs, and a comparison with preceding studies is given in table S1. Although some designs might be achieved using existing 3D printing-based methods with postfabrication assembly (16), the limitations

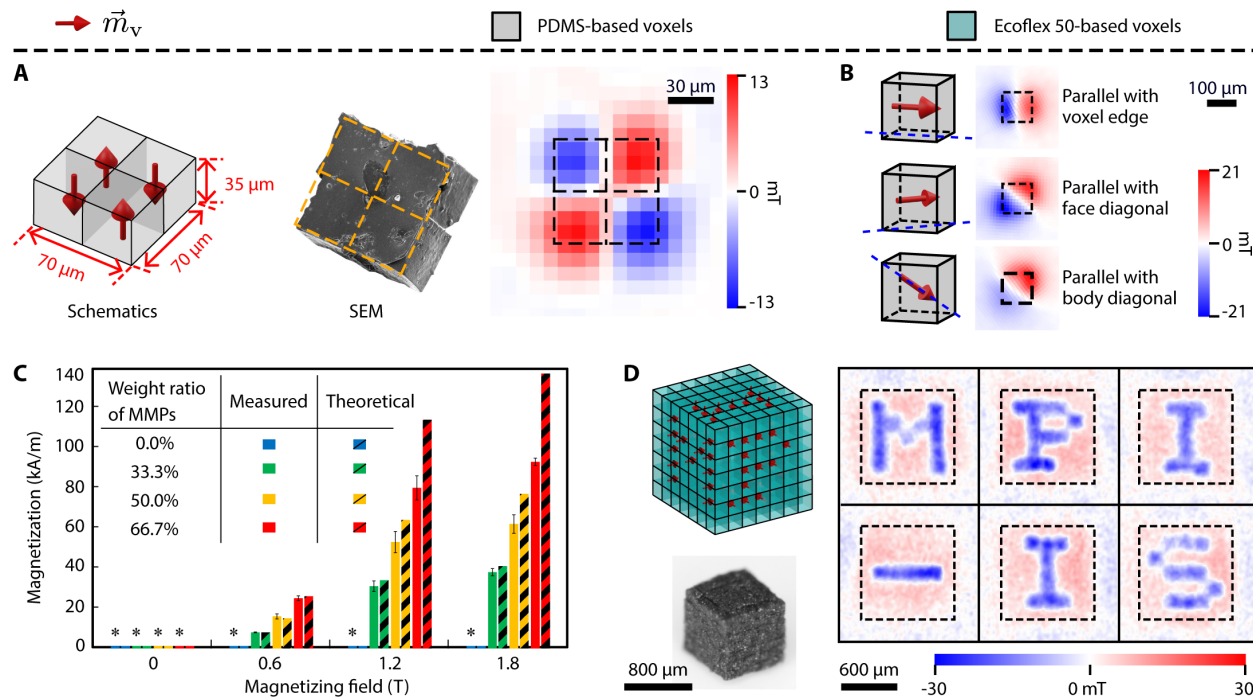


Fig. 3. Resolution characterization and creation of 3D magnetization profiles. (A) Schematic and SEM image of a checkerboard assembly. The checkerboard has a heterogeneous magnetization profile that was verified by the measurement of the normal component of its near-surface magnetic field \vec{B}_v . (B) Three 100- μm side-length cubic voxels were magnetized to have \vec{m}_v with different 3D directions. Their respective \vec{m}_v were verified by the measurement of their respective \vec{B}_v . (C) The measured and theoretical magnetization values of 100- μm side-length cubic magnetic voxels with different MMP concentrations and various magnetizing magnetic field strengths. The columns and bars represent the mean and the SD of the measurement of three samples in the same set, respectively. “**” marks the undistinguishable measurements from background noise. (D) A hollow cube has letters and symbols programmed into the magnetization profiles of its six faces. The invisible letters and symbols were revealed by imaging each face using a magnetic field imaging (magneto-optical sensor) instrument (MagView S with type B sensor, Matesy GmbH).

inherent to their working principles in multimaterial integration, resolution, miniaturization, and the coupling between magnetization profiles and geometries would still prevent them from achieving the fabrication capabilities and versatility shown in this work. In the following, we propose four devices to demonstrate the enabled critical features.

First, a cubic bare-edge frame machine was fabricated to showcase the capability of realizing abrupt 3D magnetization changes and a negative Poisson’s ratio in 3D. It was made by assembling 68 cubic voxels (Ecoflex 0050 with embedded NdFeB MMPs at 1:1 mass ratio) with 100- μm side lengths (Fig. 4A and section S4.2). In the presence of \vec{B}_c , the frame shrunk both horizontally (along both x and y axes) and vertically (along z axis), exhibiting a 3D mechanical metamaterial characteristic. Using voxels with different moduli could further tune the deformation of this structure (section S4.2).

Second, a flower-shaped machine with a sequential petal blooming response was created (Fig. 4B and section S4.3) to showcase the ability of freely integrating multiple materials together. The different building materials could have vastly different mechanical properties, e.g., Young’s moduli, to create nonuniform properties, e.g., complex stiffness distributions (28), for tailored functionalities. The machine (~1-mm diameter and 700- μm height) was made by 126 cubic magnetic voxels with 100- μm side lengths and a central hexagonal magnetic voxel. Although the magnetization profile for each of its petal is the same, its voxels were made of two kinds of elastomers: Ecoflex 0050 silicone rubber (relatively soft) and PDMS

(relatively stiff). These two voxel types with different stiffness values were used to fine-tune the stiffness distribution of the machine.

Because the shape morphing of a device is the result of the competition between the magnetic torques inducing the deformation and the resisting forces of the elastic material, tuning the stiffness distribution enables the programmability of the actuation pattern. In this case, the petals with a lower structural stiffness responded to a lower $|\vec{B}_c|$, whereas the petals with a higher structural stiffness only responded to a higher $|\vec{B}_c|$, allowing for a sequential actuation of different parts of the same device via a single global magnetic field. As a result, three petals of the machine fully opened first and the other three opened later, as $|\vec{B}_c|$ increased (Fig. 4B), which was further confirmed by a simulation analysis (section S4.3). An exemplar cantilever beam made of voxels based on five different kinds of base materials is shown in fig. S21 to show the compatibility of the proposed approach in diverse material selections. It is shown that special materials for specific applications, such as biocompatible and biodegradable gelatin voxels for biomedical applications, could also be incorporated.

Third, a starfish-shaped origami machine was fabricated (Fig. 4C and section S4.4) to demonstrate the ability of creating soft origami structures. The edge bonding technique was applied to break the bending symmetry (29) and endow the device with the ability to implement directional joint bending. The machine was made of 24 triangular flat magnetic voxels. All voxels were connected together via edge bonding. All voxels were magnetic with a 1:3 mass ratio of polymer

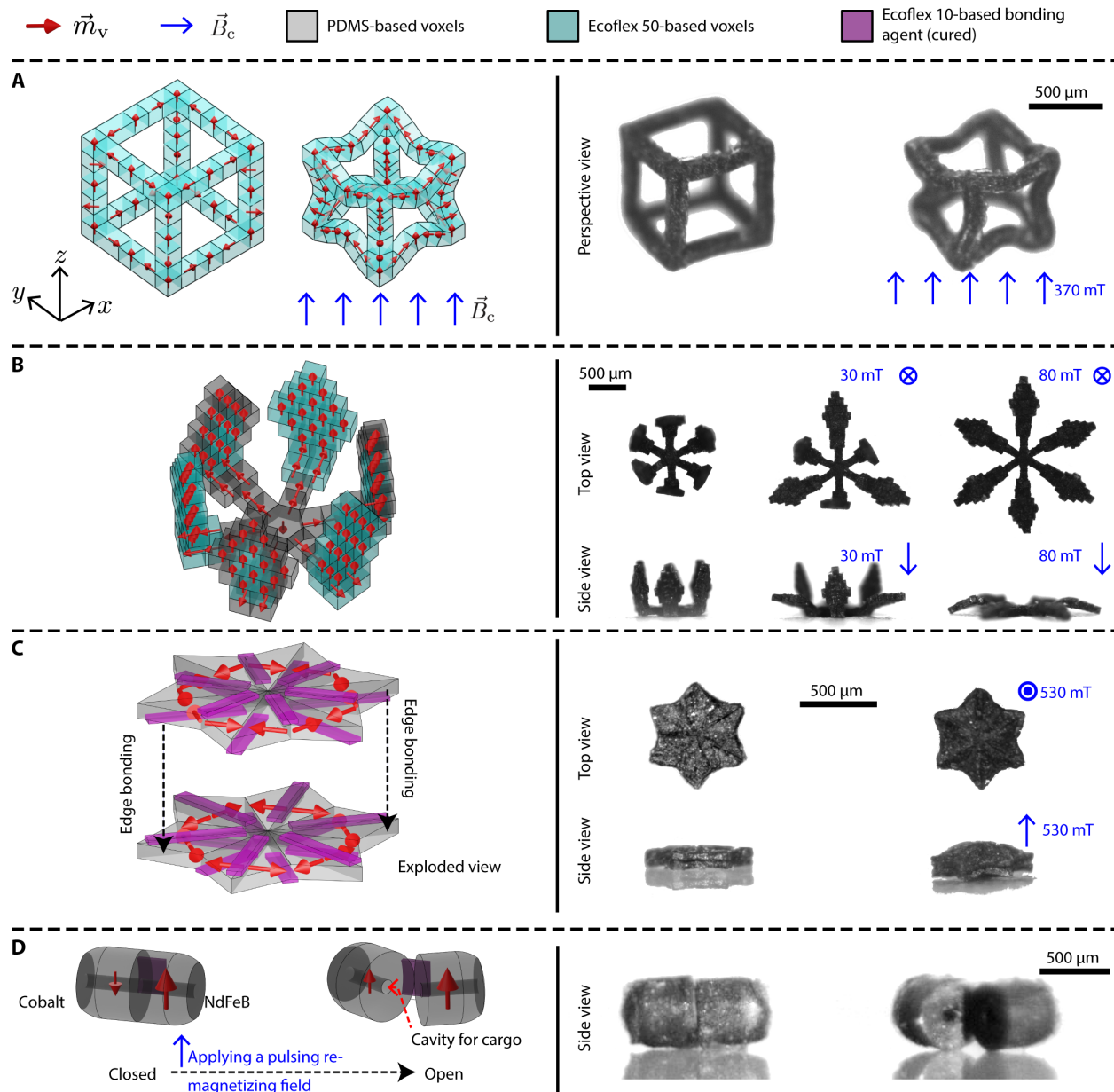


Fig. 4. Miniature magnetic soft machines demonstrating diverse characteristics. (A) A hollow cubic frame machine exhibiting 3D mechanical metamaterial characteristics with a negative Poisson’s ratio: It shrinks in all three dimensions in the presence of \vec{B}_c . (B) A flower-shaped soft machine with complex stiffness distribution. Three of its petals bloomed first in lower field strength, and the rest three bloomed later as $|\vec{B}_c|$ increased. (C) A starfish-shaped machine with directional joint bending was made by two layers of magnetic voxels. Its flat body expanded vertically and shrunk horizontally in the presence of \vec{B}_c . (D) A capsule-shaped machine with two cylindrical parts embedded with MMPs of different coercivity for reconfigurable magnetization. It was kept closed due to the attractive magnetic interactions between its two parts. After being exposed to a pulsing remagnetizing field, the part with lower coercivity MMPs reversed its magnetic moment direction, changing the magnetic interaction from attraction to repulsion, which opened the capsule. The bonding agent in face bonding connections is omitted in all schematics for easier visibility.

(PDMS) versus MMPs. In the presence of \vec{B}_c , the machine expanded vertically from its initial flat shape while concurrently shrinking horizontally.

Fourth, an untethered capsule-shaped soft machine, consisting of two cylindrical parts combined by edge bonding, was prototyped (Fig. 4D and section S4.5) to demonstrate the possibility of using multiple magnetic materials to reconfigure the soft machine by reprogramming its magnetization profile using a remote magnetic pulse (27). The machine remained closed in the nonactivated state

due to the local magnetic attraction between its two voxels. Two voxels contained two different kinds of MMP materials (NdFeB and Cobalt) with different coercivity values, respectively. To reprogram the magnetization direction of one of its voxels, a pulsing remagnetizing field (peak magnitude of 295 mT, pulse decayed to half of its peak value in 1.33 ms) was applied, which was strong and fast enough to reverse the magnetic direction of the Cobalt voxel with a lower coercivity while not affecting the NdFeB one with a higher coercivity. Thus, the local magnetic interaction was switched from

attraction to repulsion *in situ*, opening the capsule and maintaining this activated state in a stable manner even after \vec{B}_c was removed. Besides MMPs, FePt and other magnetic nanoparticles (MNPs) can also be used especially for medical applications that require biocompatible magnetic materials (fig. S1A and section S5).

Using the above critical characteristics enabled by the proposed fabrication approach, i.e., arbitrary multimaterial composition, arbitrary 3D geometry, and arbitrary programmable 3D magnetization profile, we present three new wireless miniature magnetic soft machine designs exhibiting potential biomedical functionalities. First, an intestine-inspired tubular soft peristaltic pump was developed. This pump has 37 vertically stacked circular ring-shaped horizontal slices (slice thickness, 100 μm ; outer diameter, 1.2 mm; inner diameter, 1.0 mm), each of which consists of eight arc voxels. The slices have specific magnetization profiles such that they could shrink and expand periodically with a specific phase difference (e.g., \vec{m}_v of the stacked voxels between neighboring slices was rotated by 10° in the

x - y plane) in response to a rotating \vec{B}_c in the x - y plane to create a traveling wave along the tubular soft pump (Fig. 5A and fig. S8).

The fabrication process of this machine is shown in movie S2. The traveling wave formed by the machine could pump fluids (e.g., mouse whole blood) as well as transport solid objects (e.g., a polystyrene sphere) forward or backward, depending on the direction of the traveling wave (movie S3). Because the material is hydrophobic, the capillary force does not help move the liquid. Instead, the most important factor besides the body deformation is the gravity of the liquid. To offset the influence of the gravity, control experiments were performed, and the results are represented in Fig. 5B. The machine was then mounted vertically (using the gravity) and horizontally (excluding the gravity) to translate a solid sphere (Fig. 5C), and it was controlled to pump in opposite directions, to isolate the environmental factors, such as gravity. The results conclusively show that the liquid-pumping and solid translation capabilities of the machine are indeed caused by the traveling wave-like deformation of the machine body.

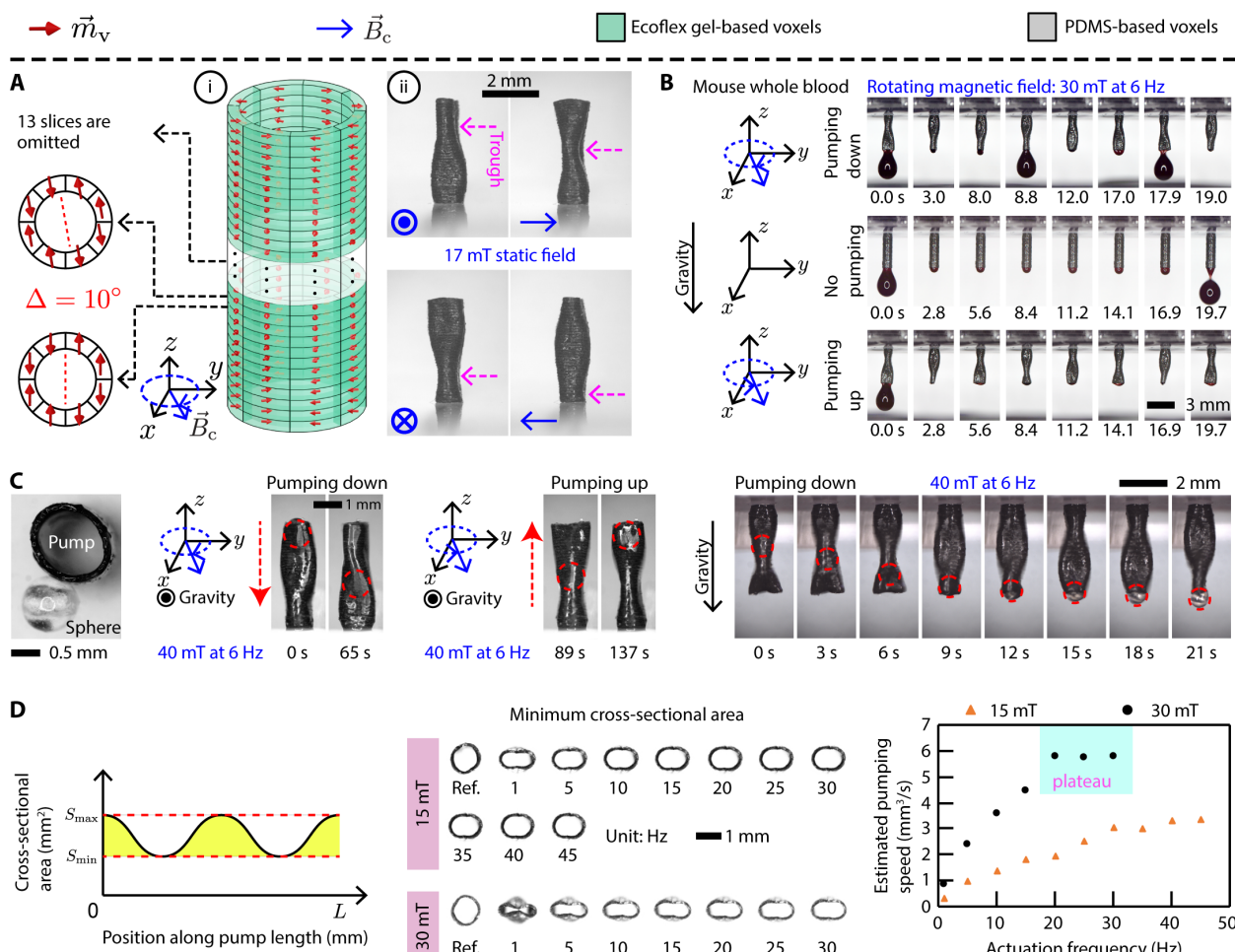


Fig. 5. Miniature wireless soft peristaltic pump with potential biomedical functionalities. (A) An intestine-inspired peristaltic soft pump. The tubular pump formed traveling wave-like deformation on its body under a rotating \vec{B}_c . (B) When placed at the bottom of a reservoir, the machine pumped mouse whole blood when its peristaltic wave propagated downward. Comparison is given between the experimental pumping results of different pumping directions. (C) The pump transported a 1-mm diameter solid polystyrene sphere in air. The sphere location is marked out by red dashed circles. The videos of all tests are available in movie S3. (D) Characterization of the pumping performance at different magnetic field strengths and rotating frequencies.

The body deformation and the pumping capacity increase with $|\vec{B}_c|$. However, when \vec{B}_c is too strong, the pump could fully close inside, i.e., its tubular structure is squeezed so much that the opposite inner wall surfaces touch each other. However, this scenario is not desired, because the inner walls of the pump may stick to each other due to the tackiness of the polymer. In that case, the peristaltic motion is slowed or even stopped. Thus, $|\vec{B}_c|$ was set to obtain a large traveling wave amplitude at a certain frequency while not causing a full closure inside the pump. Experiments were performed to characterize the correlation between the pumping speed and \vec{B}_c (Fig. 5D and section S3.1). Such wireless pump at the milliscale can mimic tubular organ peristaltic motions in organ-on-a-chip applications (30) and can create ureter models with peristalsis for surgical training. Moreover, it could potentially have future biomedical applications by forming tiny wireless implants (e.g., endometrium) inside the human body that can actively pump internal biological fluids (31).

Second, a functional hollow prolate spheroid-shaped miniature capsule with a largest diameter of 500 μm and a height of 450 μm was fabricated (Fig. 6A and section S4.7). The capsule was made up by seven ring-shaped voxels and two plate-shaped voxels. Each voxel was deformed during the magnetizing step such that it was magnetized to have a varying magnetization profile on its body. This sub-millimeter scale capsule could navigate to a targeted hard-to-reach location by surface rolling while carrying a liquid cargo, release the cargo on demand, and roll away for retrieval. In addition, it could also take liquid samples from targeted locations, useful for potential *in situ* liquid biopsy applications, especially for tumor screening (32, 33) and microbiota sampling (34).

When \vec{B}_c was applied, the capsule shrunk and caused a pressure rise within its chamber, ejecting its inner content, e.g., food dye, air, or future potential liquid drug. The net magnetic moment, \vec{m}_{net} , of the capsule allowed it to be rolled on uneven surfaces and moved over obstacles by \vec{B}_c . To demonstrate its functionalities, the machine was wirelessly rolled on an uneven surface of a stomach phantom, moved to a targeted location; expelled its enclosed liquid cargo on-demand, which was food dye here and can be replaced by drugs, genes, or imaging agents in the future; and moved out of the working environment (Fig. 6B and movie S4). Moreover, five such capsules were deployed as a team, where they moved and delivered their liquid cargoes simultaneously (Fig. 6B). Such a team of capsules could deliver higher cargo amounts and be potentially controlled independently using nonuniform magnetic fields or heterogeneous robot designs in the future (35, 36).

Such wireless miniature capsules, which can carry and administer cargoes on-demand locally, are promising for future targeted drug delivery applications in cancer, inflammation, and other diseases (10, 37, 38). Besides delivering cargoes, the liquid biopsy function of the capsule was also experimentally demonstrated by deploying an initially air-filled capsule in a food dye, activating it to take a liquid dye sample inside, controlling it to navigate to a different location, and activating it to eject the taken liquid dye sample to prove that it internalized the dye (Fig. 6C, movie S5, and section S3.2).

The diffusion of the liquid cargo carried by the capsule was also investigated. The capsule was first filled with a red food dye (with a viscosity similar to water, viscosity ≈ 0.89 centipoise at 25°C) and rolled on a surface back and forth for 30 min. Then, the capsule was activated to eject the food dye inside its chamber (Fig. 6D). The results qualitatively show that, although diffusion happened during the movement, the capsule still maintained most of its liquid cargo

after 30 min of surface rolling. Such liquid cargo diffusion could be entirely prevented if the capsule opening is fully blocked. An experiment was performed in which the capsule was filled with both liquid food dye and air (Fig. 6E). The capsule was first fully filled with liquid dye and then compressed to eject some of the liquid out. The capsule then took some air into its chamber during the process of restoring its spherical shape. After filling the air, the capsule was submerged in clear water for 30 min, during which no diffusion was observed. The ejection of the liquid cargo requires a two-step activation, i.e., the capsule was first activated to eject the air bubble blocking the opening, followed by a second activation to eject its liquid cargo.

The third functional device was an anchoring machine (outer diameter of 1.68 mm and length of 2.10 mm), which could be released, moved forward or backward, and anchored on-demand inside a tube with an internal fluidic flow (Fig. 7A and section S4.8). With wireless position control and anchoring capability without requiring a constant external energy input, such a device could be potentially used inside blood vessels in the future, to reach targeted sites deep in the body and perform minimally invasive interventions (11). The anchoring device has a diameter larger than the cross section of the targeted working space (inner diameter of the tube in this case) in its nonactuated state to form a compressive loading-based contact with the tube surface all the time for high friction and stable anchoring at the targeted location once it is deployed. Its soft elastic nature allows it to accommodate changes in the tube diameter while maintaining its anchoring position, which could potentially be useful for its deployment in blood vessels with strong pulsatile blood flow and possible vessel diameter changes (39). The hollow internal structure of the machine allows the fluid to flow through it with minimum obstruction, which prevents or minimizes the risk of tube clogging.

To demonstrate its capability of adapting to dynamically changing tube diameter, the anchoring machine was placed inside a flexible microfluidic tube (Tygon formula 2375 laboratory tubing; inner diameter of 1.6 mm, outer diameter of 3.2 mm; Merck KGaA), which was compressed by an external tip to reduce its inner diameter. The machine adapted to the dynamically changing working environment and maintained its anchoring position while resisting an internal liquid flow with a mean speed of 10 cm s^{-1} (Fig. 7B). The flow speed and the maximal compression this machine can withstand are dependent on the inner diameter, the effective radial compliance, and the material of the tube. Future changes could be made on this machine, e.g., micropatterning its outer surface, to increase its anchoring stability with higher tissue static friction.

To demonstrate its capability of delivering cargo (e.g., drugs) locally and actively in tortuous tubular environments with fluid flows, the machine was wirelessly controlled to locomote by magnetic gradient pulling inside the same microfluidic tube, which was configured into a curved shape with an end-to-end bending of about 630°. This kind of tortuous environment is difficult and risky for conventional catheters to reach (40). An aforementioned capsule was connected to the anchoring machine via a dental floss (1.8-cm long). When \vec{B}_c was applied, the anchoring machine shrunk to a smaller size than the inner diameter of the tube and was pulled against the liquid flow in the tube by the spatial gradient of \vec{B}_c ($\nabla \vec{B}_c$), which was created by an external permanent magnet. When \vec{B}_c was removed, the device restored its initial shape due to its stored elastic energy, anchored itself inside the tube, and resisted the liquid flow with a mean flow speed of 5 cm s^{-1} (Fig. 7C). The capsule was then

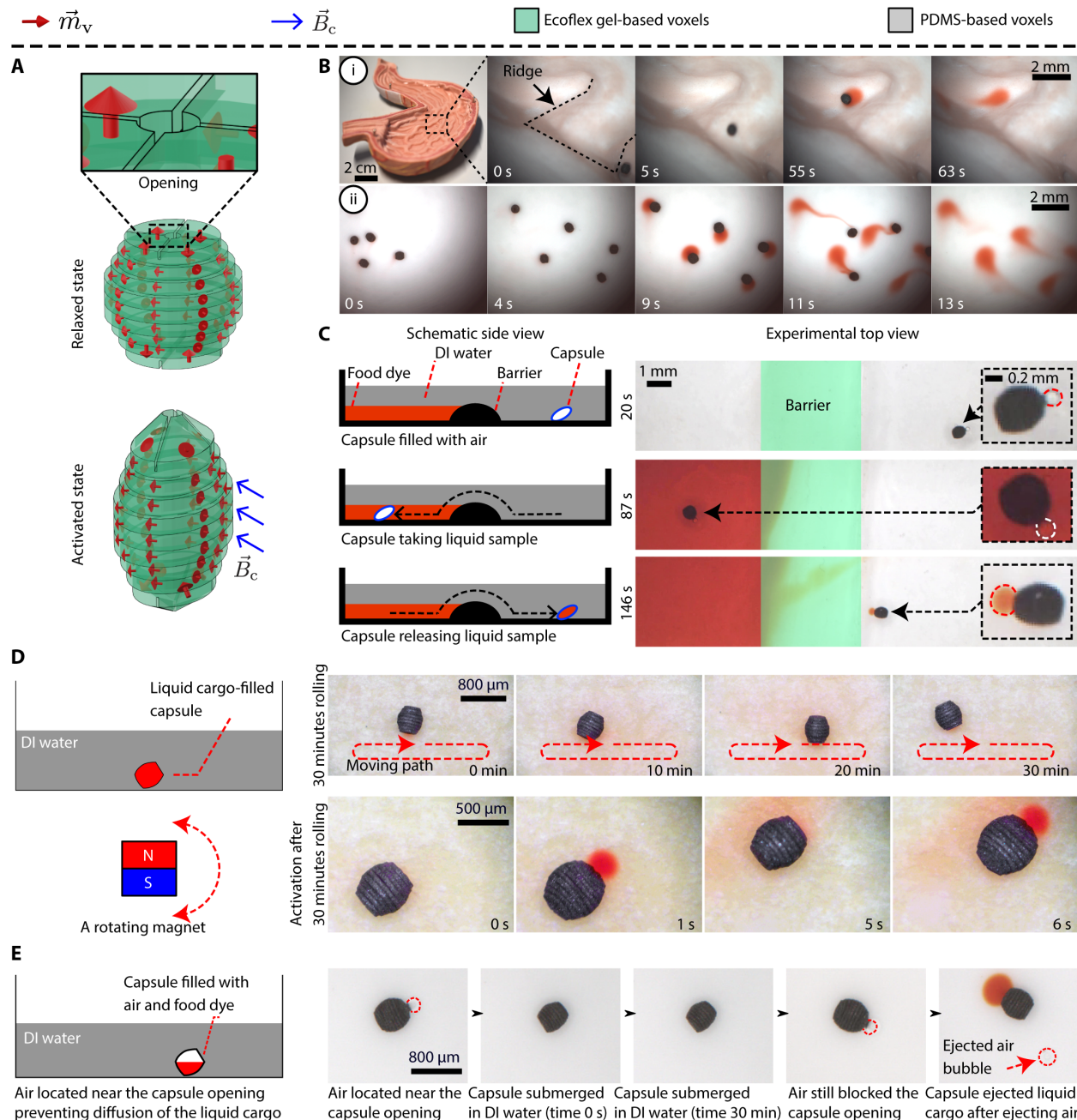


Fig. 6. Miniature wireless soft capsule with potential biomedical functionalities. (A) Schematics of the capsule, ejecting its internal liquid cargo on-demand through its designed top opening. (B) The capsule rolled on a stomach phantom surface and released a food dye on-demand. Five capsules were moved and activated together to release the internal dummy drug liquids. (C) The capsule took fluid samples for future potential *in situ* liquid biopsy applications. (D) The capsule was initially filled with red food dye and then submerged in clear water. It rolled on a surface back and forth for 30 min. Then, the capsule was activated to eject the content in its chamber. (E) The capsule was filled with both liquid food dye and air. It was submerged in clear water for 30 min to observe diffusion. Next, it was activated to eject the air in its chamber and then the liquid food dye.

activated to compress and release its liquid cargo (a food dye) it carried. Videos of these two experiments are available in movie S6. The inner diameter of the tube used in this experiment is within the range of the clinical measurements of the average lumen diameter (41) of the human coronary arteries.

The anchoring machine was used to carry therapeutic stem cells (42) to demonstrate its potential toward vascular regeneration

applications, such as in the case of ischemia and peripheral artery diseases (43, 44). In this regard, biocompatible, two-photon lithography-based 3D-printed microcages that can entrap mesenchymal stem cells (MSCs) were heterogeneously integrated to the anchoring device's surface contacting regions as a cell scaffold, for confining the cells during the potential delivery process (Fig. 7D). MSCs were enclosed to the cages as shown in fig. S4. The cell suspension was

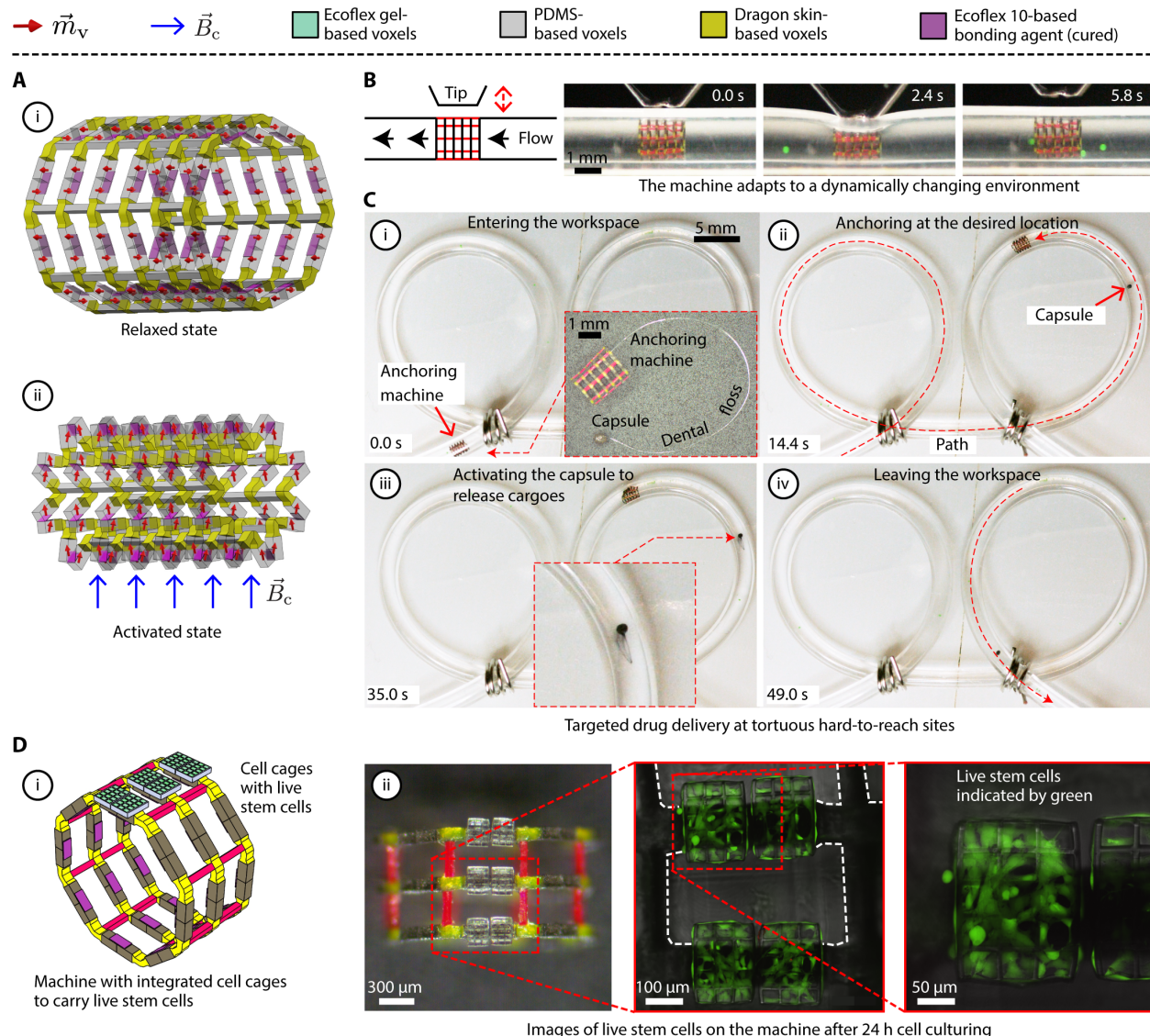


Fig. 7. Wireless miniature soft anchoring machine with potential biomedical functionalities. (A) A surface-anchoring machine anchored and released on-demand inside a tubular phantom with a fluid (water) flow: (i) relaxed state and (ii) activated state. (B) The machine adapted to a working environment with a dynamically changing diameter. (C) Anchoring and cargo delivery demonstration in a synthetic tube. (i) The machine entered the workspace. During the locomotion, the anchoring machine was at the activated state all the time. (ii) The anchoring machine restored to the relaxed state and anchored at the desired location. (iii) The soft capsule machine attached to the anchoring machine was activated to release the liquid cargo (dye here) at the targeted location. (iv) The anchoring machine was activated again and pulled away from the workspace. (D) Live stem cell integrated machine demonstration toward future vascular regeneration applications. (i) Microcages that entrap MSCs were heterogeneously integrated to the anchoring machine's surface-contacting regions as a cell scaffold. (ii) The machine integrated live stem cells into its body. The zoomed fluorescence optical images, taken 24 hours after the cell culturing, showed that the cells lived and spread out on the cage surface with no noticeable toxic effect. The bonding agent in face bonding connections is omitted in all schematics for easier visibility.

dropped from the top of the cages, and MSCs were allowed to sediment into the cages. To increase the adhesion of MSCs to the cages, the device was kept in $25 \mu\text{g ml}^{-1}$ fibronectin solution before cell seeding. Adhesion of the MSCs to the microcages and their subsequent spreading on the cage surface were demonstrated without observing any noticeable toxic effect exerted by the device or the microcages for 24 hours (Fig. 7D). Confining stem cells on microcarriers with open structures has become a widely adopted strategy to locally deliver the cells, in which case the stem cells would adhere to their carriers during transportation and proliferate, migrate, and

differentiate after reaching the target site (42, 45, 46). Currently, the release of cells relies on natural migration of cells. As cells grow and proliferate, more surface is needed to spread. Notwithstanding, stimuli-responsive materials could be used to coat the inner part of the cages to trigger release in the form of cell sheet as one strategy in the future. This delivery strategy could also enable carrying drugs or drug depots that need to be released for an extended period of time (limited by the maximum possible volume of the loaded drug) at a targeted location. When the drug is depleted, the device could be released from its anchoring location for retrieval.

Table 1. Fabrication durations and voxel types and numbers of all prototyped soft devices. The shown values refer to the time needed to magnetize and assemble voxels into each machine prototype. Curing of the bonding agents happens simultaneously during the assembly. A post-assembly curing of the machine on a hot plate or in an oven is performed to maximize the performance. This post-assembly curing does not require human intervention and is not counted in the durations here.

Prototyped devices	Fabrication duration (hours)	Number of voxels		
		Total	Magnetic	Nonmagnetic
3D ring	5	50	32	18
Hollow cubic frame	6	68	68	0
Flower-shaped machine	6	127	127	0
Starfish-shaped machine	4	24	24	0
Capsule-shaped machine	2	4	2	2
Peristaltic pump	8	296	296	0
Capsule	1	9	9	0
Anchoring device	10	184	96	88

The fabrication duration for all reported machines is given in Table 1. There exists a fundamental competition between the resolution and the size of a fabricated device, due to the additive manufacturing nature of this approach. Here, we intentionally limit the voxel number in a device to be no more than 500 to balance the fabrication resolution and duration. The reported approach intends to address the immediate fabrication challenge in the field of magnetic soft machines at the smaller end of the size spectrum, i.e., several millimeters to hundreds of micrometers. This size scale is most relevant to the targeted biomedical application (11) of the functional machines demonstrated in this work. The reported approach can be adapted to create larger and more complex devices with a trade-off between the sizes of individual voxels and the overall device size. Such a trade-off ensures that the desired resolution is achieved at a reasonable duration in the fabrication process (see the “Automation and mass producibility” section).

CONCLUSIONS

The above biomedical functionalities shown on the reported miniature soft magnetic machines are enabled by the extended design freedom in material, geometry, and magnetization profile, which is a result of the bottom-up nature of the reported fabrication approach. Their mechanical, structural, and magnetic designs can be further optimized for solving specific clinical problems in the future. With respect to materials, the platinum-catalyzed silicones used in this research have been used to coat medical catheters (47), but more-biocompatible voxel materials, e.g., gelatin, can be used to coat or directly make the voxels (section S5). In addition, magnetic nanomaterials, e.g., ferromagnetic FePt nanoparticles that have been shown to be biocompatible (48), can also be used to render the reported devices more applicable to *in vivo* clinical applications. The reported fabrication approach addresses an immediate challenge in miniature soft magnetic robotics by relaxing the fabrication constraints in material, geometry, and magnetization. The reported exemplar machines showcase the enriched design space using this approach. It is envisioned that this work may inspire future machines enabled by the improved design freedom with advanced functionalities and applicabilities to address real-world challenges.

MATERIALS AND METHODS

Voxel fabrication

Voxels of various materials and shapes were fabricated by casting polymer with optional MMPs into shape-defining molds and cured in batches. Before this step, positive molds with protruding features were designed in Solidworks (Dassault Systèmes) and created using two-photon polymerization (TPP; Photonic Professional GT, Nanoscribe GmbH). TPP can create high-fidelity 3D geometries for fast-prototyping and quick iterations. The photoresists IP-S and IP-Q (Nanoscribe GmbH) were used. PDMS (Sylgard 184, Dow Corning, base and curing agents mixed at 5:1 mass ratio) was cast to the positive molds to create negative molds with corresponding concave features. Vacuum degassing removed trapped air. These negative molds were silanized by trichloro(1H,1H,2H,2H-perfluoroctyl) silane (Merck KGaA) to facilitate polymer cross-linking and voxel releasing. All molds could be used repeatedly. This voxel fabrication process is illustrated in fig. S1A.

General photolithography technique could also be used to fabricate molds. However, it is unnecessary to fabricate batches of molds due to their reusability, whereas the iteration of the mold design is more critical. In addition, creating 3D geometries is challenging for the photolithography technique. Thus, it is considered as an option only when a design is compatible.

The selected base materials were mixed with the selected MMPs or MNPs, e.g., neodymium-iron-boron (NdFeB; MQP-15-7, Magnequench, average diameter of 5 μm), at a certain mass ratio, which could be tuned for different $|\vec{m}_v|$ (Fig. 3C). The specific mass ratios and the material selections for all machines are given in section S4. The fluidic mixture was cast on the negative molds and vacuum degassed to remove trapped air. Excess mixture was removed using razor blades. The mixture cured into voxels with the designed geometric features. The curing temperature and time specified by the polymer manuals were followed. These cured voxels were taken out by tweezers or needles from the molds.

Previously reported fabrication methods (13,16, 23) can fabricate some of the voxels, but these existing methods only support a single recipe of material to bear the programmed magnetization profiles. Multimaterial integration with inscribed magnetization profiles is a key advantage of the proposed approach.

Base materials used here include platinum-catalyzed silicone (Ecoflex series, including 0010-0050 and Gel), PDMS, urethane plastic, and gelatin (section S5). The properties of these materials were characterized via tensile tests of samples according to ASTM D412 on a universal testing machine (Instron 5942; Instron, Norwood, MA). Results are given in table S2. Besides the material selections, the geometries of individual voxels could also be designed. Figure S1C shows some example voxels with various geometries. Being able to make various voxel geometries could potentially save time and cost in fabrication, because (i) they make better geometric profiles for a device, e.g., it is difficult to create a smooth surface using generic cubic voxels for the peristaltic pump; and (ii) when feasible, a larger voxel with nongeneric geometries could replace many generic voxels in a device to improve efficiency, e.g., the employment of ring voxels in the capsule saves time in fabrication in comparison with the case of using many generic cubic voxels.

Magnetizing process

Magnetic voxels were positioned at desired 3D orientations using assistant jigs and magnetized by a vibrating sample magnetometer (VSM; EZ7, Microsense) to program \vec{m}_v with 3D strength and orientation (fig. S1D). The magnetizing field \vec{B}_m had a strength of 1.8 T unless otherwise specified. Concurrently, $|\vec{m}_v|$ was controlled by the MMPs' concentration in the voxels as well as $|\vec{B}_m|$. Exemplary voxels with different MMPs' concentration and magnetized along different directions were imaged in fig. S2A. The magnetic properties of the bare MMPs were also measured (fig. S2B).

The VSM created \vec{B}_m within the gap between its two parallel circular plates. The direction of \vec{B}_m was perpendicular to the circular plates, and its strength was controlled by the terminal of the VSM. The voxels were fixed to their corresponding orientations in a jig, and the jig was fixed to a cubic acrylic plate that is 1 cm wide. This cubic acrylic plate was clamped by the two circular plates of the VSM, leaving the voxels located at the geometric center of the gap. \vec{B}_m was then generated to magnetize the voxels. The VSM ramped up to a desired $|\vec{B}_m|$ at 0.2 T s^{-1} , stayed at the desired strength (1.8 T for example) for 2 s, and then ramped down to 0 at -0.2 T s^{-1} . The specific $|\vec{B}_m|$ used for each reported machine can be found in section S4.

The assistant jigs could also fix the deformation of a voxel or a group of voxels to program a varying magnetization profile on the body of a voxel or a group of voxels. Voxels were often magnetized before being assembled for maximum fabrication versatility. However, in some designs, some voxels could be assembled first and then magnetized for improved efficiency, such as the capsule in Fig. 6 and the anchoring device in Fig. 7. The two approaches were both demonstrated using the exemplar 3D ring (Fig. 2 and fig. S11).

Jig-assisted assembly

Voxels were assembled together with the bonding agent applied to connect neighboring voxels (see the “Jig-assisted face bonding” and “Jig-assisted edge bonding” sections for detailed descriptions of the bonding process). Both the position and the orientation of each voxel were controlled in the assembly process using assistant jigs, resulting in a 3D geometry and magnetization profile of the final machine. Such mechanical fixing helps overcome the magnetic interaction between voxels, preventing them from collapsing into each other or flying away during fabrication.

We used face bonding and edge bonding to bond voxels together to form synthetic 3D soft machines. Bonding agents were used to

form the intervoxel bonds that fix each voxel at its designated position. The bonding agents were selected as the uncured liquid soft elastomers that could cure in contact with the neighboring voxels. In the rare cases where such an appropriate elastomer is not available, mechanical interlocking structures could be applied. Various kinds of glues, such as universal glues and optical glues, could also be used as alternatives. The energy dissipation induced by the mechanical interlocking structures and the compatibility of various glues to the voxels need to be investigated in the future. Details of the fabrication process for the reported machines, including the material designs and the magnetizing field strength in each case, can be found in section S4.

Assembly was performed under a stereomicroscope (ZEISS Stemi 508, Carl Zeiss Microscopy GmbH) with a magnification value between $\times 6.3$ and $\times 50$. The zoom and focus could be easily adjusted by the rotary knobs located at its both sides. Tweezers (5-SA Outils Rubis SA, Switzerland) or iron needles (Agani 30G needles, Terumo) were used as the primary tools to perform the assembly. A 0.03-mm-diameter copper wire was nested within a Seque/Pro capillary tip (Bio-Rad Laboratories) as a tool to apply bonding agent. In addition, magnetized iron needles were occasionally used to distinguish the \vec{m}_v direction of a voxel. All the instruments are low cost and easy to access in academia and industry.

Resting hands on a still surface during assembly ameliorated hand vibrations. The surface could be the benchtop on which the microscope is placed upon. This manner makes the assembly a doable operation for average people. When manipulating voxels using tweezers, it is recommended to only move one tweezer at a time while using the other tweezer (held by another hand) to hold the jig or the already-assembled part of the device. In this way, most maneuvering is reduced to translational movement, further simplifying the process.

Design and fabrication of the assistant jigs

Reusable assistant jigs provide guideline and reference in fabrication and help fix the positions and orientations of the voxels, ensuring the fabrication precision and repeatability (section S2). The 2D jigs are similar to the molds in mold casting, with concave features that accommodate corresponding parts. Dimensions of the jigs were based on the parts made of multiple voxels. The size of the concave features was designed to be slightly larger than the outline of the corresponding parts to make sure the parts can be inserted. The jigs were created via TPP directly or mold casting. In the latter, the molds were made by casting PDMS (Sylgard 184, Dow Corning, base and curing agents mixed at 5:1 mass ratio) to the structures created by TPP to form negative molds. The 3D jigs have out-of-plane features to support the 3D parts by creating an additional working plane. They were directly made via TPP with special objectives (10 \times and 25 \times , Nanoscribe GmbH) designed for large features (compared with the traditional TPP size scale). One typical example is the jig used to assemble the 3D ring (Fig. 2).

The jig designs for all machines are included in section S4. The reported designs are, by no means, the only feasible ones. Jig designs were mostly heuristically created and based on experiences as well as trial and error. The design and optimization of jigs are beyond the scope of this study and warrant a separate following investigation.

Jig-assisted face bonding

Face bonding brings two voxels together “face-to-face” with bonding agent in the middle to form a continuous structure without

joints. The amount of bonding agent was negligible because excess agent was squeezed away by pushing two voxels together. There was no observable difference between a face-bonded and a bulk-casted beam (section S6).

There are three approaches (fig. S3A): (i) Only one voxel was placed in the jig. (ii) The other voxel was also placed in the jig with a distance left between the voxels. (iii) The two voxels were placed in the jig with their ends left outside, especially for soft voxels. A nested copper wire worked as a tool to dip into the bonding agent and take some at its tip. The wire was moved close to the voxel until the liquid bonding agent touched the surface. Then, the wire was moved away. The bonding agent at the voxel surface spread across the face area automatically. Next, the second voxel was (i) placed in the jig or (ii) moved in the jig toward the first voxel. In the third case, (iii) the parts of the two voxels outside were pushed into the jig. Excess of the bonding agent was squeezed out and removed by a tweezer or a needle. Face bonding is symmetric and does not have a direction preference in bending.

Jig-assisted edge bonding

Edge bonding joined neighboring voxels by forming an explicit joint and creating an asymmetric connection. The bonding agent was applied at one side of the contacting faces of two voxels. Specifically, two voxels could be placed in a jig that has an extra space on the side or the bottom (fig. S3B). The bonding agent was cast into this pocket, and excess bonding agent was removed by a tweezer or a needle. The amount of bonding agent in edge bonding was controlled by the shape of the assistant jig.

With no bonding agent between their contacting faces, the voxels could easily disengage from each other during deformation. As an example in Fig. 1B, the bonding agent applied at the top edge fixed the voxels at the top side, making it much easier for the joint to open from the bottom side. With this design, the voxels disengaged and the joint opened when \vec{B}_c pointed up. Such an open joint (the middle case in Fig. 1B, “Edge bonding”) allowed a large deformation to be achieved using a relatively small torque. When \vec{B}_c was reversed, the voxels compressed into each other and the joint remained closed. Such a closed joint (the third case in Fig. 1B, “Edge bonding”) forced the whole soft body to bend and made the bending more difficult, resulting in smaller deformations under the same torque magnitude. Conventionally, a large deformation needs a strong actuating magnetic field or soft body material. This asymmetric edge bonding approach inspired by a previous study (29) enables a large deformation at a relatively weak actuating magnetic field, giving more freedom for designing shape-morphing devices. It is not designed to bear much load along its preferred deformation direction.

Post-assembly curing

After voxels were assembled, the whole device was stored at a designated temperature for the curing of the bonding agents. These temperatures were determined by the curing requirements provided by the corresponding manufacturers of the selected bonding agents. Nonmagnetic hot plates and an oven were used to provide an environment at a certain temperature for this step.

Magnetic actuation

The machines were placed inside their designated test setups and observed with an optical microscope. Handheld permanent magnets (Neodymium, nickel-plated, Supermagnete) produced a magnetic

field in arbitrary 3D directions within the workspace. The magnetic actuation and control using electromagnets have been extensively discussed previously (18) and are not the focuses here. The sample deformation and motion were captured with a video camera (Point Grey Research Inc.) and a high-speed camera (Phantom Cinemag II v641). Each sample was tested multiple times without any observable signs of performance variation or deterioration. Specific experimental setup and procedure for each reported machine are available in section S4.

Loading stem cells to the anchoring soft machine

Human adipose-derived MSCs [American Type Culture Collection (ATCC)] were cultured in a humidified, 37°C, 5% CO₂ environment using 75-cm² polystyrene cell culture flasks containing MSC basal medium (ATCC) supplemented with MSC growth kit for low serum (ATCC), 2% fetal bovine serum (Gibco), penicillin (25 UI ml⁻¹), and streptomycin (25 µg ml⁻¹). Cells were split before they reached to 80% confluence by 0.25% trypsin-EDTA (Gibco) solution.

To capture the stem cells, microcages 3D-printed by TPP were heterogeneously integrated to an anchoring machine (fig. S4A), which is one-half of the six-ring anchoring machine shown in Fig. 7. The cage was made of biocompatible commercial IP-Visio photopolymer (Nanoscribe GmbH) that is specially designed for cell culture and tissue engineering. The cage was designed with a tenon so that it could fit into the corresponding mortise on the anchoring machine. During the assembly, we first applied a small amount of uncured silicone elastomer (Ecoflex 0010) into the mortise of the voxel before the cage was inserted. Before seeding the cells, the whole device was put into 1× phosphate-buffered saline (PBS) solution and sterilized under UV for 1 hour. After the sterilization, the whole device was incubated in 25 µg ml⁻¹ fibronectin solution in 1× PBS for 2 hours at 37°C to increase the cell adhesion to the microcages. After the fibronectin treatment, the whole device was washed with PBS, and the cells in suspension were seeded from the top (in 50-µl volume) with a density of 1.5 × 10⁶ cells/ml. The device with the entrapped cells was then transferred to humidified, 37°C, 5% CO₂ environment.

To investigate the viability of cells after 24 hours of cell entrapment, a LIVE/DEAD viability/cytotoxicity kit was used to stain live and dead cells based on the manufacturer’s fluorescence microscopy protocol. Briefly, a vial of live green was thawed and mixed with the dead red component to create 2× working solution, which was then added to the well containing the anchoring device with an equal volume of growth medium. The device and cells were incubated with the solution for 30 min at room temperature before imaging. A spinning disk confocal microscope (Nikon Instruments Inc., Eclipse Ti-E) was used to image the live and dead cells.

Cell adhesion and retention in the microcages could be further controlled by creating an artificial cell niche within the cages in the future. Decorating the inner surface of the microcages with natural extracellular matrix-derived cell-adhesive peptides and proteins can enable regulating the cell fate and behavior (42). Also, recapitulating the physical properties of native stem cell environments by tuning the mechanical properties of the cages can support the stability and retention of the cells during the device transport.

Automation and mass producibility

This work establishes a fabrication approach and provides exemplar machines to showcase its fabrication capabilities. This work opens

the door to a design and fabrication platform that can be optimized and automated in the future by our and other groups. Automatizing such fabrication approach is nontrivial and warrants a separate study.

Scientifically, automation requires investigations on the automatic handling and bonding of diverse soft building blocks, 3D real-time object recognition and tracking, etc. at the sub-millimeter scale. Considering the state of the art, substantial progress needs to be made in all these areas. Practically, the current form of the reported fabrication approach already satisfies the need for fast prototyping and quickly iterating designs in research and low-volume manufacturing in specific applications. In particular, targeted biomedical applications require a small number of highly customized machines tailored for individual patient, with the possibility of integrating patient-derived biomaterials. Different from nanorobots deployed in swarms, the machines shown here exhibit stronger single-device functionalities and will work individually or in a small team.

The reported approach creates magnetic soft machines at the size scale from several millimeter down to tens of micrometers. It can be adapted for larger devices with a balance obtained between the sizes of individual voxels and the overall device. A larger device often does not require the same resolution for every part of its body compared with a smaller one. Thus, making appropriate voxels larger can help attain the device functionalities at a reasonable fabrication cost. Future design optimizations can minimize the voxel number while maintaining the functionalities, broadening the suitable scenarios of this approach.

SUPPLEMENTARY MATERIALS

robotics.sciencemag.org/cgi/content/full/6/53/eabf0112/DC1

Materials and Methods

Section S1. Measurement of voxel magnetization

Section S2. Evaluation of the fabrication precision and tolerance to fabrication variances

Section S3. Characterization of the demonstrated functional soft machines

Section S4. Design, assembly process, and experimental details of the reported devices

Section S5. Compatibility of the proposed method with multiple kinds of materials

Section S6. Comparison between assembled and cast samples

Section S7. Extended discussion on mass production

Fig. S1. Illustrations of the mold casting and magnetizing steps of the proposed fabrication approach and its versatility.

Fig. S2. Magnetic characterization of the MMPs used in this work.

Fig. S3. Schematic illustrations of the face and edge bonding methods.

Fig. S4. Loading live stem cells to the microcages heterogeneously integrated to the anchoring soft machine top surface.

Fig. S5. Quantitative characterization of the assembly precision.

Fig. S6. Mechanical characterizations of the materials and comparisons against the neo-Hookean model.

Fig. S7. Finite element simulation-based investigation of the effect of the fabrication imperfections on the two-ring anchoring machine performance.

Fig. S8. Observations of the shape morphing of the peristaltic pump.

Fig. S9. Liquid biopsy of the capsule.

Fig. S10. Analysis of the magnetic attraction force on device deformation.

Fig. S11. Illustration of the jig-assisted fabrication of the exemplar 3D ring.

Fig. S12. Designs of the hollow cubic frame, simulation verification, fabrication process, and cargo transport demonstration.

Fig. S13. Designs of the flower-shaped machine, simulation verification, and fabrication process.

Fig. S14. Designs of the starfish-shaped machine, simulation verification, and fabrication process.

Fig. S15. Designs of the capsule-shaped machine and its fabrication process.

Fig. S16. Schematic illustrations of the electrical setup for the pulsing magnetic field.

Fig. S17. Designs of the peristaltic pump and illustrations of its fabrication process.

Fig. S18. Experimental setup to make a rotating magnetic field for the peristaltic pump.

Fig. S19. Designs of the capsule and its fabrication process.

Fig. S20. Designs of the anchoring machine and illustrations of its fabrication process.

Fig. S21. Exemplar cantilever beam made of voxels based on five different kinds of materials.

Fig. S22. Shape morphing comparison between assembled and cast cantilever beams.

Table S1. Comparison of the proposed fabrication method with the ones previously reported in the literature.

Table S2. Material characterization of various kinds of materials used in the reported machines.

Movie S1. Video recordings of the representative steps in the fabrication of the exemplar 3D ring machine.

Movie S2. Video recordings of the representative steps in the fabrication of the functional peristaltic pump machine.

Movie S3. Experimental results of a small-scale magnetic soft peristaltic pump that pumps mouse whole blood and transport a solid sphere in a rotating uniform magnetic field.

Movie S4. Experimental results of the reported miniature magnetic soft capsules.

Movie S5. Experimental results, including an experimental trial and a control trial, of a miniature magnetic soft capsule taking liquid samples and demonstrate potentials for future liquid biopsy applications.

Movie S6. Experimental results of a small-scale magnetic soft anchoring machine.

Reference (49)

REFERENCES AND NOTES

- Z. Ren, W. Hu, X. Dong, M. Sitti, Multi-functional soft-bodied jellyfish-like swimming. *Nat. Commun.* **10**, 2703 (2019).
- Y. Dong, J. Wang, X. Guo, S. Yang, M. O. Ozen, P. Chen, X. Liu, W. Du, F. Xiao, U. Demirci, B. F. Liu, Multi-stimuli-responsive programmable biomimetic actuator. *Nat. Commun.* **10**, 4087 (2019).
- A. Nojomi, H. Arslan, K. Lee, K. Yum, Bioinspired 3D structures with programmable morphologies and motions. *Nat. Commun.* **9**, 3705–3715 (2018).
- H. Lu, M. Zhang, Y. Yang, Q. Huang, T. Fukuda, Z. Wang, Y. Shen, A bioinspired multilegged soft millirobot that functions in both dry and wet conditions. *Nat. Commun.* **9**, 3944 (2018).
- J. Zhang, Y. Guo, W. Hu, R. H. Soon, Z. S. Davidson, M. Sitti, Liquid crystal elastomer-based magnetic composite films for reconfigurable shape-morphing soft miniature machines. *Adv. Mater.* **33**, e2006191 (2021).
- J. Zhang, E. Diller, Tetherless mobile micrograsping using a magnetic elastic composite material. *Smart Mater. Struct.* **25**, 11LT03 (2016).
- S. E. Chung, X. G. Dong, M. Sitti, Three-dimensional heterogeneous assembly of coded microgels using an untethered mobile microgripper. *Lab Chip* **15**, 1667–1676 (2015).
- T. G. Leong, C. L. Randall, B. R. Benson, N. Bassik, G. M. Stern, D. H. Gracias, Tetherless thermobiocochically actuated microgrippers. *Proc. Natl. Acad. Sci. U.S.A.* **106**, 703–708 (2009).
- A. Ghosh, C. Yoon, F. Ongaro, S. Scheggi, F. M. Selaru, S. Misra, D. H. Gracias, Stimuli-responsive soft untethered grippers for drug delivery and robotic surgery. *Front. Mech. Eng.* **3**, 7 (2017).
- S. Fusco, M. S. Sakar, S. Kennedy, C. Peters, R. Bottani, F. Starsich, A. Mao, G. A. Sotiriou, S. Pané, S. E. Pratsinis, D. Mooney, B. J. Nelson, An integrated microrobotic platform for on-demand, targeted therapeutic interventions. *Adv. Mater.* **26**, 952–957 (2014).
- M. Sitti, H. Ceylan, W. Hu, J. Giltinan, M. Turan, S. Yim, E. Diller, Biomedical applications of untethered mobile milli/microrobots. *Proc. IEEE* **103**, 205–224 (2015).
- J. Li, B. Esteban-Fernandez de Avila, W. Gao, L. Zhang, J. Wang, Micro/nanorobots for biomedicine: Delivery, surgery, sensing, and detoxification. *Sci. Robot.* **2**, eaam6431 (2017).
- T. Xu, J. Zhang, M. Salehizadeh, O. Onaizah, E. Diller, Millimeter-scale flexible robots with programmable three-dimensional magnetization and motions. *Sci. Robot.* **4**, eaav4494 (2019).
- D. Garcia-Gonzalez, Magneto-visco-hyperelasticity for hard-magnetic soft materials: Theory and numerical applications. *Smart Mater. Struct.* **28**, 085020 (2019).
- M. Sitti, *Mobile Microrobotics* (MIT Press, Cambridge, MA, 2017).
- Y. Kim, H. Yuk, R. K. Zhao, S. A. Chester, X. H. Zhao, Printing ferromagnetic domains for untethered fast-transforming soft materials. *Nature* **558**, 274–279 (2018).
- J. A.-C. Liu, J. H. Gillen, S. R. Mishra, B. A. Evans, J. B. Tracy, Photothermally and magnetically controlled reconfiguration of polymer composites for soft robotics. *Sci. Adv.* **5**, eaaw2897 (2019).
- W. Hu, G. Z. Lum, M. Mastrangeli, M. Sitti, Small-scale soft-bodied robot with multimodal locomotion. *Nature* **554**, 81–85 (2018).
- W. Gao, L. L. Wang, X. Z. Wang, H. Z. Liu, Magnetic driving flowerlike soft platform: Biomimetic fabrication and external regulation. *ACS Appl. Mater. Inter.* **8**, 14182–14189 (2016).
- G. Z. Lum, Z. Ye, X. Dong, H. Marvi, O. Erin, W. Hu, M. Sitti, Shape-programmable magnetic soft matter. *Proc. Natl. Acad. Sci. U.S.A.* **113**, E6007–E6015 (2016).
- E. Diller, J. Zhuang, G. Z. Lum, M. R. Edwards, M. Sitti, Continuously distributed magnetization profile for millimeter-scale elastomeric undulatory swimming. *Appl. Phys. Lett.* **104**, 174101 (2014).

22. Y. Li, Z. Qi, J. Yang, M. Zhou, X. Zhang, W. Ling, Y. Zhang, Z. Wu, H. Wang, B. Ning, H. Xu, W. Huo, X. Huang, Origami NdFeB flexible magnetic membranes with enhanced magnetism and programmable sequences of polarities. *Adv. Funct. Mater.* **29**, 1904977 (2019).
23. J. Kim, S. E. Chung, S. E. Choi, H. Lee, J. Kim, S. Kwon, Programming magnetic anisotropy in polymeric microactuators. *Nat. Mater.* **10**, 747–752 (2011).
24. J. Tang, C. Yao, Z. Gu, S. Jung, D. Luo, D. Yang, Super-soft and super-elastic DNA robot with magnetically driven navigational locomotion for cell delivery in confined space. *Angew. Chem. Int. Ed. Engl.* **59**, 2490–2495 (2020).
25. R. Dreyfus, J. Baudry, M. L. Roper, M. Fermigier, H. A. Stone, J. Bibette, Microscopic artificial swimmers. *Nature* **437**, 862–865 (2005).
26. A. M. Yousefi, B. J. Smucker, A. Naber, C. Wytrick, C. Shaw, K. Bennett, S. Szekely, C. Focke, K. A. Wood, Controlling the extrudate swell in melt extrusion additive manufacturing of 3D scaffolds: A designed experiment. *J. Biomater. Sci. Polym. Ed.* **29**, 195–216 (2018).
27. J. Cui, T. Y. Huang, Z. Luo, P. Testa, H. Gu, X. Z. Chen, B. J. Nelson, L. J. Heyderman, Nanomagnetic encoding of shape-morphing micromachines. *Nature* **575**, 164–168 (2019).
28. N. W. Bartlett, M. T. Tolley, J. T. B. Overvelde, J. C. Weaver, B. Mosadegh, K. Bertoldi, G. M. Whitesides, R. J. Wood, A 3D-printed, functionally graded soft robot powered by combustion. *Science* **349**, 161–165 (2015).
29. S. Wu, Q. Ze, R. Zhang, N. Hu, Y. Cheng, F. Yang, R. Zhao, Symmetry-breaking actuation mechanism for soft robotics and active metamaterials. *ACS Appl. Mater. Inter.* **11**, 41649–41658 (2019).
30. S. Jalili-Firoozinezhad, F. S. Gazzaniga, E. L. Calamari, D. M. Camacho, C. W. Fadel, A. Bein, B. Swenor, B. Nestor, M. J. Cronce, A. Tovaglieri, O. Levy, K. E. Gregory, D. T. Breault, J. M. S. Cabral, D. L. Kasper, R. Novak, D. E. Ingber, A complex human gut microbiome cultured in an anaerobic intestine-on-a-chip. *Nat. Biomed. Eng.* **3**, 520–531 (2019).
31. A. Nakai, K. Togashi, T. Yamaoka, T. Fujiwara, H. Ueda, T. Koyama, H. Kobayashi, T. Kagimura, S. Fujii, J. Konishi, Uterine peristalsis shown on cine MR imaging using ultrafast sequence. *J. Magn. Reson. Imaging* **18**, 726–733 (2003).
32. Y. Yoshioka, N. Kosaka, Y. Konishi, H. Ohta, H. Okamoto, H. Sonoda, R. Nonaka, H. Yamamoto, H. Ishii, M. Mori, K. Furuta, T. Nakajima, H. Hayashi, H. Sugisaki, H. Higashimoto, T. Kato, F. Takeshita, T. Ochiya, Ultra-sensitive liquid biopsy of circulating extracellular vesicles using ExoScreen. *Nat. Commun.* **5**, 3591 (2014).
33. E. Crowley, F. Di Nicolantonio, F. Loupakis, A. Bardelli, Liquid biopsy: Monitoring cancer-genetics in the blood. *Nat. Rev. Clin. Oncol.* **10**, 472–484 (2013).
34. G. Aragonès, M. Colom-Pellicer, C. Aguilar, E. Guiu-Jurado, S. Martínez, F. Sabench, J. A. Porras, D. Riesco, D. D. Castillo, C. Richart, T. Auguet, Circulating microbiota-derived metabolites: A liquid biopsy? *Int. J. Obes.* **44**, 875–885 (2020).
35. E. Diller, J. Giltinan, M. Sitti, Independent control of multiple magnetic microrobots in three dimensions. *Int. J. Robot. Res.* **32**, 614–631 (2013).
36. X. G. Dong, M. Sitti, Controlling two-dimensional collective formation and cooperative behavior of magnetic microrobot swarms. *Int. J. Robot. Res.* **39**, 617–638 (2020).
37. X. Z. Chen, M. Hoop, N. Shamsudhin, T. Huang, B. Özkal, Q. Li, E. Sirinçil, F. Mushtaq, L. D. Tizio, B. J. Nelson, S. Pané, Hybrid magnetoelectric nanowires for nanorobotic applications: Fabrication, magnetoelectric coupling, and magnetically assisted in vitro targeted drug delivery. *Adv. Mater.* **29**, 1605458 (2017).
38. S. P. Woods, T. G. Constantinou, Wireless capsule endoscope for targeted drug delivery: Mechanics and design considerations. *I.E.E.E. Trans. Biomed. Eng.* **60**, 945–953 (2013).
39. F. Hansen, D. Bergqvist, P. Mangell, Å. Rydén, B. Sonesson, T. Länne, Non-invasive measurement of pulsatile vessel diameter change and elastic properties in human arteries: A methodological study. *Clin. Physiol.* **13**, 631–643 (1993).
40. R. R. Attaran, S. Butman, M. R. Movahed, Going around the bend: Deep inspiration facilitates difficult stent delivery in the native coronary arteries. *Tex. Heart Inst. J.* **38**, 270–274 (2011).
41. J. T. Dodge Jr., B. G. Brown, E. L. Bolson, H. T. Dodge, Lumen diameter of normal human coronary arteries. Influence of age, sex, anatomic variation, and left ventricular hypertrophy or dilation. *Circulation* **86**, 232–246 (1992).
42. I. C. Yasa, A. F. Tabak, O. Yasa, H. Ceylan, M. Sitti, 3D-printed microrobotic transporters with recapitulated stem cell niche for programmable and active cell delivery. *Adv. Funct. Mater.* **29**, 1808992 (2019).
43. A. O. J. Fakoya, New delivery systems of stem cells for vascular regeneration in ischemia. *Front. Cardiovasc. Med.* **4**, 7 (2017).
44. A. Liew, T. O'Brien, Therapeutic potential for mesenchymal stem cell transplantation in critical limb ischemia. *Stem Cell Res. Ther.* **3**, 28 (2012).
45. T. Wei, J. Liu, D. Li, S. Chen, Y. Zhang, J. Li, L. Fan, Z. Guan, C. M. Lo, L. Wang, K. Man, D. Sun, Development of magnet-driven and image-guided degradable microrobots for the precise delivery of engineered stem cells for cancer therapy. *Small* **16**, e1906908 (2020).
46. S. Jeon, S. Kim, S. Ha, S. Lee, E. Kim, S. Y. Kim, S. H. Park, J. H. Jeon, S. W. Kim, C. Moon, B. J. Nelson, J. Y. Kim, S.-W. Yu, H. Choi, Magnetically actuated microrobots as a platform for stem cell transplantation. *Sci. Robot.* **4**, eaav4317 (2019).
47. W. J. Bae, J. B. Choi, K. S. Kim, S. J. Kim, H. J. Cho, U. S. Ha, S. H. Hong, J. Y. Lee, S. W. Kim, AB168. Evaluation of the biocompatibility of packing materials for a catheter. *Transl. Androl. Urol.* **4**, AB168 (2015).
48. V. M. Kadiri, C. Bussi, A. W. Holle, K. Son, H. Kwon, G. Schütz, M. G. Gutierrez, P. Fischer, Biocompatible magnetic micro- and nanodevices: Fabrication of FePt nanopropellers and cell transfection. *Adv. Mater.* **32**, e2001114 (2020).
49. R. Zhang, S. Wu, Q. Ze, R. Zhao, Micromechanics study on actuation efficiency of hard-magnetic soft active materials. *J. Appl. Mech.* **87**, 091008 (2020).

Acknowledgments: We thank N. Krishna-Subbaiah for assistance with TPP, A. Shiva for assistance with tensile tests, M. Dudek for assistance with scanning electron microscopy, and Y. Yu for assistance with biological materials. **Funding:** J.Z. thanks the Alexander von Humboldt Foundation for financial support. This work is funded by the Max Planck Society, European Research Council (ERC) Advanced Grant SoMMoR project with grant no. 834531, and German Research Foundation (DFG) Soft Material Robotic Systems (SPP 2100) Program with grant no. 2197/3-1. **Author contributions:** J.Z., Z.R., W.H., and M.S. proposed and designed the research. J.Z., Z.R., W.H., and R.H.S. performed the experiments and analyzed the data. Z.R., W.H., and Z.L. performed and analyzed the simulations. I.C.Y., Z.R., and W.H. performed and analyzed the stem cell experiments. J.Z., Z.R., W.H., I.C.Y., and M.S. wrote the paper. All authors discussed the results and edited or commented on the manuscript. **Competing interests:** Max Planck Innovation has filed a patent application for the inventions in this work. J.Z., Z.R., W.H., and M.S. are listed as inventors. The other authors declare that they have no competing interests. **Data and materials availability:** All data needed to evaluate the conclusions in the paper are present in the paper or the Supplementary Materials.

Submitted 28 September 2020

Accepted 29 March 2021

Published 28 April 2021

10.1126/scirobotics.abf0112

Citation: J. Zhang, Z. Ren, W. Hu, R. H. Soon, I. C. Yasa, Z. Liu, M. Sitti, Voxelated three-dimensional miniature manetic soft machines via multimaterial heterogeneous assembly. *Sci. Robot.* **6**, eabf0112 (2021).